ALICE/96-36
Internal Note/TPC/SIM
31 October 1996

ALICE TPC Slow Simulator

Marek Kowalski
Institute of Nuclear Physics, Cracow
kowalski@hpion-1.ifj.edu.pl

Abstract

In this note the algorithm for the detailed simulations of the ALICE TPC data is presented. The space point resolutions in both $r\varphi$ and z directions, as well as the width of clusters are obtained for different parameters of the FE electronics and readout-chamber geometry.

1 Physics of TPC Monte Carlo

In this section the physical processes occuring in the TPC gas volume are described, as well as the details of the signal collection on the readout-chambers are presented.

1.1 Ionization in gas

The distance between collisions of a charged particle with the gas atoms is described by an exponential distribution (see for example [1])

$$P(s) = \frac{1}{D} \exp \frac{-s}{D} ,$$

where s is the distance between two successive collisions and D is the mean distance between collisions. The D parameter is obtained from

$$D = \frac{1}{N_{prim} \cdot f(\beta\gamma)} ,$$

where N_{prim} is the number of primary electrons per cm produced by a minimum ionizing particle (MIP), and $f(\beta\gamma)$ is the ionization curve.
The values of N_{prim} for different gases are shown in the Table 1.1.

Gas	E_i (eV)	W_i (eV)	N_{prim} i.p./cm	N_{tot} i.p./cm
Ne	21.6	36	12	39
Ar	15.8	26	29.4	94
CH_4	13.1	28	16	53
CO_2	13.7	33	34	91

Table 1: Ionization properties of several gases used in TPCs. E_i is the ionization energy, W_i is the energy required to produce an electron–ion pair, N$prim$ (N_{tot}) is the number of primary (total number of) electrons per unit length. All numbers are taken from [2].

The energy loss data for Ar-CH_4 (90/10) [3, 4] are shown in Fig. 1, together with the parametrization of the form

$$\frac{I}{I_\circ} = \frac{P_1}{\beta^{P_4}} \cdot \left\{ P_2 - \beta^{P_4} - \ln \left[P_3 + \frac{1}{(\beta\gamma)^{P_5}} \right] \right\} ,$$

proposed by the ALEPH Collaboration [4], where $P_1 - P_5$ are the free parameters. As shown in [3], the behaviour of the Ne-based mixtures is very similar.
The interaction cross section of a charged particle with a gas atom obeys the $1/E^2$ rule, thus the $1/E^2$ distribution has been used for the energy loss generator, neglecting the effects of the atom shell structure.

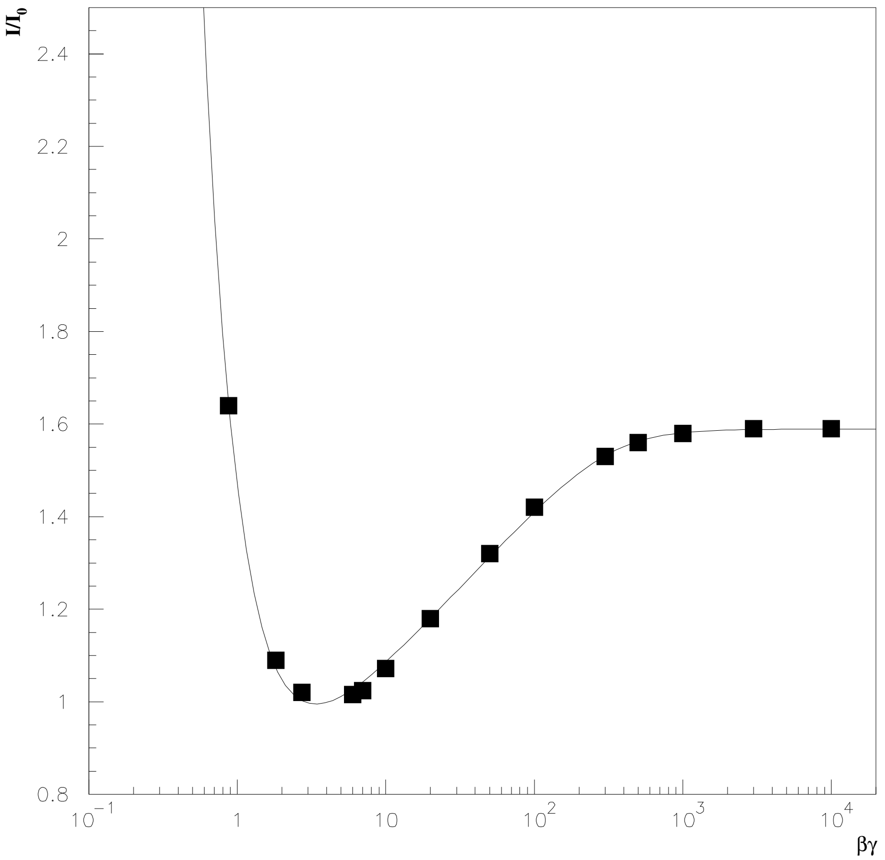

Figure 1: Energy loss data for Ar-CH_4 90/10.

1.2 Production of secondary electrons

With sufficient kinetic energy, the primary electron can ionize atoms and produce secondary electrons, creating an electron cluster. The total number of electrons in such a cluster is given by

$$N_{tot} = \frac{E_{tot}}{W_i} + 1 \,,$$

where E_{tot} is the energy loss in a given collision and W_i is defined as in Table 1.1. The clusters were assumed to be point-like, and no distinction between primary and secondary electrons has been made. This seems to be justified, as most of the fractional energy losses in a given step are small (on the average about 3–4 electrons are produced in a single collision). Thus the practical range of the primary electron in gas, (which is responsible for the intrinsic size of the cluster), is small, compared with the length scale of diffusion during the drift towards readout-chambers. The practical range of an electron in Ne is shown in Fig. 2.

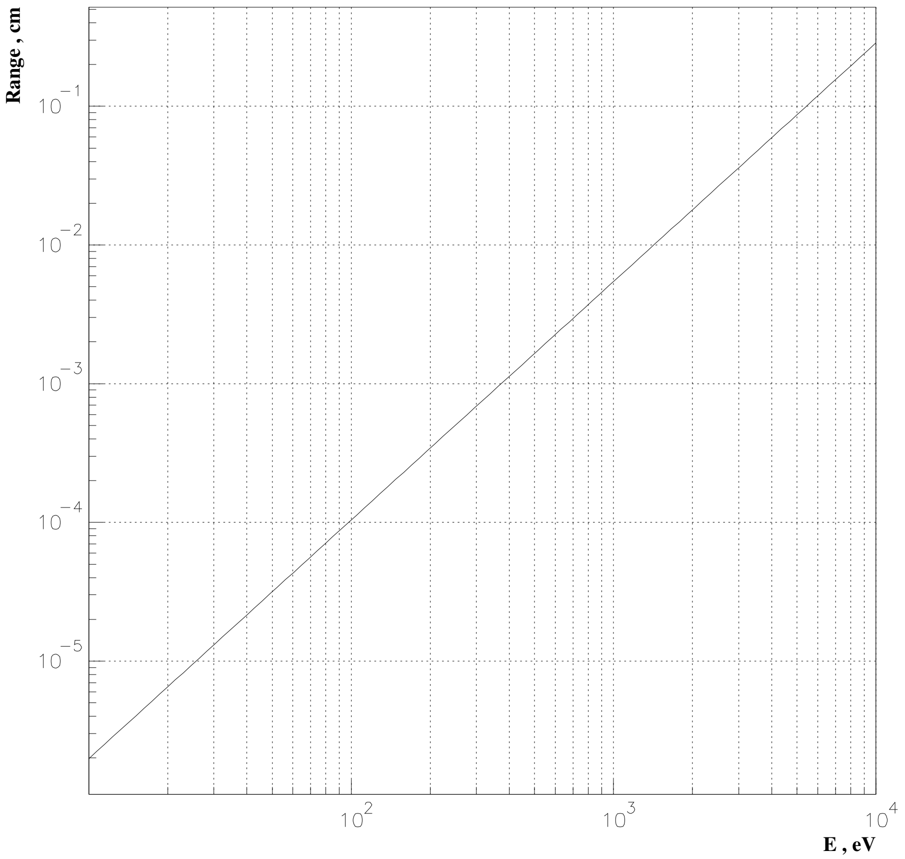

Figure 2: Practical range of electron in Neon, parametrization taken from [2].

1.3 Diffusion of electrons

The diffusion of electrons can be described using the 3-D Gaussian distribution

$$P(\delta x,\delta y,\delta z)=\frac{1}{\sqrt{2\pi}\sigma_T}exp\left[-\frac{(\delta x)^2}{2\sigma_T^2}\right]\cdot\frac{1}{\sqrt{2\pi}\sigma_T}exp\left[-\frac{(\delta y)^2}{2\sigma_T^2}\right]\cdot\frac{1}{\sqrt{2\pi}\sigma_L}exp\left[-\frac{(\delta z)^2}{2\sigma_L^2}\right],$$

$\delta x\,(y,z)=x\,(y,z)-x_0\,(y_0,z_0)$, (x_0,y_0,z_0) being the electron creation point,

$$\sigma_T=D_T\sqrt{L_{drift}}$$

$$\sigma_L = D_L \sqrt{L_{drift}} \ ,$$

where $\sigma_{T(L)}$ are the diffusion constants in the transverse and longitudinal direction respectively, and L_{drift} is the drift length.

1.4 Electron capture

The process of electron capture in the TPC gas has been studied by the NA49 Collaboration. It has been concluded that the probability for the electron to be captured by an O_2 molecule is 1% per 1 m drift per 1 ppm of O_2 [5]. The results presented in this note have been obtained without taking the electron capture into account. This will be the subject of further studies.

1.5 E $\times$ B effect near the sense wires

It has been assumed that the electric and magnetic fields in the drift volume are uniform and parallel. This, however, is not true close to the sense wires, where the electric field becomes radial. Thus the electrons experience a shift along the wire direction (due to the Lorentz force). If an electron enters the readout-chamber at the point (x_0, y_0), it is displaced in the x-direction (assuming that the wires are placed along x-axis). The new x-position of the electron is then given by

$$x = x_0 + \omega\tau \cdot (y - y_0) \ ,$$

where y is the y-coordinate of the wire on which an electron is collected, and $\omega\tau$ is the tangent of Lorentz angle.

1.6 Gas gain fluctuations

The gas gain fluctuations can be described, following [1], by the exponential distribution

$$P(q) = \frac{1}{\overline{q}} \cdot \exp - \frac{q}{\overline{q}} \ ,$$

where $\overline{q}$ is the average avalanche amplitude.

1.7 Charge induced on pads and pad response function (PRF)

An electron collected on the sense wire induces a charge on the pad plane. This charge is integrated over the pad area. What characterizes the readout-chamber and determines the intrinsic resolution is the pad response function (PRF). If the charge induced on the pad plane has the distribution given by $Q(x,y)$, the PRF is defined as

$$PRF(x,y) = \int_{y-\frac{L}{2}}^{y+\frac{L}{2}} \int_{x-\frac{W}{2}}^{x+\frac{W}{2}} Q(x',y')dx'dy' \ ,$$

where L, W are the pad length and width respectively. There have been many calculations on the charge induced on the pad plane (see for example [4, 6]). An example of the induced charge distribution is shown in Fig. 3. A detailed discussion

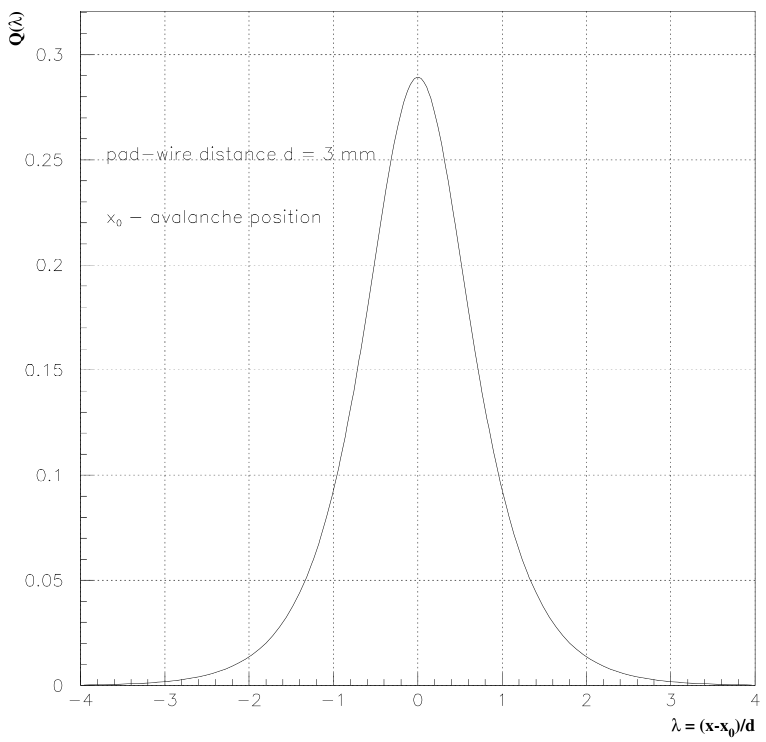

Figure 3: One-dimensional distribution of the induced charge, calculated according to [6].

of the calculation of the PRF for the ALICE TPC can be found in [7].

1.8 Shaping and sampling time signal

The time signal is obtained by folding the avalanche with the shaping function of the preamp/shaper. This signal is then sampled with a given frequency. In these simulations a 3σ truncated Gaussian has been used to describe the preamp/shaper response.

1.9 Digitization of signal

The analog signal, obtained by the integration of signals created by single electrons is digitized, assuming that the most probable maximal charge per cluster is equal to 70 ADC counts, the r.m.s of the electronic noise, σ_{noise}, is 2.5 ADC counts and a zero-suppression threshold of 5 ADC counts, as obtained for the NA49 FE electronics [5]. As the result of the simulations described above, 2-dimensional clusters in a pad–time-bucket space are obtained.

2 Results of simulations

In this section the space-point resolutions and the widths of the cluster obtained for different widths of the shaping function, different sampling frequencies and different widths of the PRF and pads are presented. The numerical values of the parameters used in the simulations are listed in Table 2.

Item	Value
Drift velocity	2.5 cm/μs
$\omega\tau$	0.125
$\sigma_T = \sigma_L$	250 μm/$\sqrt{cm}$
Electric field	400 V/cm
Magnetic field	0.2 T

Table 2: Parameter values used in the TPC simulations.

2.1 Space-point resolution and cluster width as function of FWHM of pream/shaper response and sampling time

These calculations have been performed for a high P_t tracks (3 GeV/c) in order to get rid of the effects connected with the track curvature ($\tan\alpha$ effect). Thus, one can study only the dependence on the electronics parameters and a dip angle ($\tan\lambda$ effect). The results for a pad-row radius of 110 cm are presented in Tables 3 – 5, for a pad-row radius of 175 cm in Tables 6 – 8, and for a pad-row radius of 240 cm in Tables 9 – 11.

2.2 Space-point resolution and cluster width as function of PRF and pad widths

For further studies the FWHM of 250 ns and a sampling time of 200 ns have been chosen. This is a compromise between the required resolution and cluster width on one hand and the data volume and the cluster shape on the another. One should keep in mind, that too narrow FWHM leads to probing signals from single electrons and thus to clusters exhibiting the fluctuation pattern. A smaller sampling time increases the data volume without significant improvement of the resolution. Calculation have been performed for tracks almost parallel to the readout plane ($\theta = 6^\circ$) in order to study only the effects of the track curvature ($\tan\alpha$). The results for P_t=3 GeV/c are shown in Table 12, for P_t=200 MeV/c in Tables 13 – 14 and for P_t=100 MeV/c in Tables 15 – 16. They can be used in further studies concerning the design of the readout-chamber geometry.

3 Acknowledgements

I am very grateful to Robert Brockmann, Nick van Eijndhoven, Hans-Gerhard Fischer, Rainer Renfordt, Andrzej Rybicki, and Karel Šafařík for many helpful suggestions and discussions.

References

[1] G. F. Knoll, Radiation Detection and Measurements, New York : Wiley, 1979.

[2] F. Sauli, CERN 77-09, 1977

[3] I. Lehrhaus et al., IEEE Trans. Nucl. Sci. **30** (1983) 50.

[4] W. Blum, L. Rolandi, Particle Detection with Drift Chambers, Springer-Verlag, Berlin, Heidelberg, 1993.

[5] H. G. Fischer, private communication.

[6] E. Mathieson et al., NIM **227** (1984) 227 and references therein.

[7] A. Rybicki, ALICE/95-29, Int. Note 1995.

FWHM ns	Sampling time ns					
	100	125	150	175	200	250
180	820 μm 4.7 mm	860 μm 5.0 mm	850 μm 5.0 mm			
200	830 μm 4.9 mm	860 μm 5.0 mm	850 μm 5.1 mm			
250		850 μm 5.2 mm	870 μm 5.3 mm	900 μm 5.5 mm	940 μm 5.6 mm	990 μm 5.9 mm
300		850 μm 5.5 mm	870 μm 5.6 mm	910 μm 5.7 mm	920 μm 5.8 mm	
350				910 μm 6.0 mm	940 μm 6.1 mm	990 μm 6.4 mm

Table 3: Resolution (upper row) and cluster width (lower row) in z, $\theta = 6°$, $R_{pad} =$ 110 cm.

FWHM ns	Sampling time ns					
	100	125	150	175	200	250
180	1630 μm 5.7 mm	1640 μm 5.7 mm	1620 μm 5.8 mm			
200	1630 μm 5.7 mm	1640 μm 5.8 mm	1630 μm 5.9 mm			
250		1650 μm 6.0 mm	1640 μm 6.1 mm	1650 μm 6.2 mm	1700 μm 6.3 mm	1740 μm 6.5 mm
300		1650 μm 6.2 mm	1630 μm 6.3 mm	1640 μm 6.4 mm	1670 μm 6.5 mm	
350				1650 μm 6.6 mm	1690 μm 6.8 mm	1750 μm 7.0 mm

Table 4: Resolution (upper row) and cluster width (lower row) in z, $\theta = 28°$, $R_{pad} = 110$ cm.

FWHM ns	Sampling time ns					
	100	125	150	175	200	250
180	2170 μm 7.0 mm	2180 μm 7.1 mm	2190 μm 7.1 mm			
200	2180 μm 7.0 mm	2170 μm 7.1 mm	2170 μm 7.2 mm			
250		2180 μm 7.2 mm	2170 μm 7.3 mm	2150 μm 7.4 mm	2190 μm 7.5 mm	2220 μm 7.7 mm
300		2170 μm 7.4 mm	2180 μm 7.5 mm	2150 μm 7.6 mm	2200 μm 7.7 mm	
350				2130 μm 7.8 mm	2190 μm 7.9 mm	2200 μm 8.1 mm

Table 5: Resolution (upper row) and cluster width (lower row) in z, $\theta = 43°$, $R_{pad} = 110$ cm.

FWHM ns	Sampling time ns					
	100	125	150	175	200	250
180	830 μm 4.9 mm	840 μm 4.9 mm	890 μm 5.0 mm			
200	820 μm 4.9 mm	850 μm 5.0 mm	890 μm 5.1 mm			
250		860 μm 5.2 mm	890 μm 5.3 mm	900 μm 5.4 mm	900 μm 5.6 mm	1010 μm 5.8 mm
300		830 μm 5.5 mm	900 μm 5.6 mm	900 μm 5.7 mm	890 μm 5.8 mm	
350				890 μm 5.9 mm	920 μm 6.1 mm	990 μm 6.4 mm

Table 6: Resolution (upper row) and cluster width (lower row) in z, $\theta = 6°$, $R_{pad} = 175$ cm.

FWHM ns	Sampling time ns					
	100	125	150	175	200	250
180	1410 μm 5.4 mm	1450 μm 5.4 mm	1450 μm 5.5 mm			
200	1410 μm 5.4 mm	1450 μm 5.5 mm	1460 μm 5.6 mm			
250		1460 μm 5.9 mm	1450 μm 5.8 mm	1460 μm 5.9 mm	1460 μm 6.0 mm	1560 μm 6.3 mm
300		1450 μm 5.9 mm	1440 μm 6.0 mm	1450 μm 6.1 mm	1460 μm 6.2 mm	
350				1440 μm 6.4 mm	1460 μm 6.5 mm	1560 μm 6.8 mm

Table 7: Resolution (upper row) and cluster width (lower row) in z, $\theta = 28°$, $R_{pad} = 175$ cm.

FWHM ns	Sampling time ns					
	100	125	150	175	200	250
180	2000 μm 6.4 mm	2030 μm 6.5 mm	2010 μm 6.6 mm			
200	1990 μm 6.5 mm	2020 μm 6.6 mm	2020 μm 6.7 mm			
250		2010 μm 6.7 mm	2040 μm 6.8 mm	2040 μm 6.9 mm	2000 μm 7.0 mm	2020 μm 7.3 mm
300		2000 μm 6.9 mm	2020 μm 7.0 mm	2010 μm 7.1 mm	1970 μm 7.2 mm	
350				2030 μm 7.3 mm	2020 μm 7.4 mm	2030 μm 7.7 mm

Table 8: Resolution (upper row) and cluster width (lower row) in z, $\theta = 43°$, $R_{pad} = 175$ cm.

FWHM ns	Sampling time ns					
	100	125	150	175	200	250
180	830 μm 4.8 mm	870 μm 4.9 mm	870 μm 5.0 mm			
200	830 μm 4.8 mm	870 μm 5.0 mm	870 μm 5.1 mm			
250		870 μm 5.1 mm	890 μm 5.3 mm	900 μm 5.4 mm	940 μm 5.5 mm	1020 μm 5.8 mm
300		860 μm 5.4 mm	880 μm 5.5 mm	910 μm 5.6 mm	940 μm 5.8 mm	
350				890 μm 5.9 mm	940 μm 6.0 mm	990 μm 6.3 mm

Table 9: Resolution (upper row) and cluster width (lower row) in z, $\theta = 6°$, $R_{pad} =$ 240 cm.

FWHM ns	Sampling time ns					
	100	125	150	175	200	250
180	1560 μm 5.0 mm	1590 μm 5.1 mm	1570 μm 5.2 mm			
200	1560 μm 5.1 mm	1580 μm 5.2 mm	1560 μm 5.3 mm			
250		1570 μm 5.4 mm	1560 μm 5.5 mm	1600 μm 5.6 mm	1610 μm 5.7 mm	1630 μm 6.1 mm
300		1560 μm 5.7 mm	1560 μm 5.8 mm	1600 μm 5.9 mm	1600 μm 6.0 mm	
350				1590 μm 6.1 mm	1610 μm 6.2 mm	1620 μm 6.6 mm

Table 10: Resolution (upper row) and cluster width (lower row) in z, $\theta = 28°$, $R_{pad} = 240$ cm.

FWHM ns	Sampling time ns					
	100	125	150	175	200	250
180	1930 μm 5.9 mm	1940 μm 5.9 mm	1950 μm 6.0 mm			
200	1930 μm 5.8 mm	1940 μm 5.9 mm	1940 μm 6.0 mm			
250		1950 μm 6.1 mm	1940 μm 6.2 mm	1950 μm 6.3 mm	1940 μm 6.4 mm	1980 μm 6.7 mm
300		1930 μm 6.3 mm	1940 μm 6.4 mm	1920 μm 6.6 mm	1920 μm 6.7 mm	
350				1930 μm 6.8 mm	1920 μm 6.9 mm	1980 μm 7.2 mm

Table 11: Resolution (upper row) and cluster width (lower row) in z, $\theta = 43°$, $R_{pad} = 240$ cm.

PRF width mm	Pad pitch mm			
	2.5	3.5	4.5	5.5
2.5	660 μm 4.8 mm	680 μm 4.9 mm	700 μm 5.0 mm	730 μm 5.1 mm
3.5	630 μm 5.3 mm	650 μm 5.4 mm	680 μm 5.4 mm	690 μm 5.6 mm
4.5	630 μm 5.9 mm	630 μm 6.0 mm	660 μm 6.0 mm	660 μm 6.1 mm
5.5	630 μm 6.5 mm	630 μm 6.6 mm	640 μm 6.7 mm	660 μm 6.7 mm

Table 12: Resolution (upper row) and cluster width (lower row) in $r\varphi$, $\theta = 6°$, $P_t = 3000$ MeV/c, $R_{pad} = 110$ cm. The results for $\theta = 6°$ and $R_{pad} = 240$ cm are almost the same as for $\theta = 6°$ and $R_{pad} = 110$ cm and thus not shown in the separate Table.

PRF width mm	Pad pitch mm			
	2.5	3.5	4.5	5.5
2.5	570 μm 5.0 mm	580 μm 5.1 mm	590 μm 5.1 mm	590 μm 5.1 mm
3.5	570 μm 5.6 mm	580 μm 5.6 mm	580 μm 5.6 mm	580 μm 5.7 mm
4.5	560 μm 6.2 mm	570 μm 6.2 mm	570 μm 6.2 mm	580 μm 6.3 mm
5.5	570 μm 6.8 mm	570 μm 6.9 mm	580 μm 6.9 mm	580 μm 7.0 mm

Table 13: Resolution (upper row) and cluster width (lower row) in $r\varphi$, $\theta = 6°$, $P_t = 200$ MeV/c, $R_{pad} = 110$ cm.

PRF width mm	Pad pitch mm			
	2.5	3.5	4.5	5.5
2.5	1010 μm 5.5 mm	1010 μm 5.5 mm	1020 μm 5.6 mm	1010 μm 5.6 mm
3.5	1000 μm 5.9 mm	1000 μm 6.0 mm	1000 μm 6.0 mm	1010 μm 6.1 mm
4.5	1000 μm 6.5 mm	1000 μm 6.6 mm	1000 μm 6.6 mm	1000 μm 6.7 mm
5.5	1000 μm 7.1 mm	1000 μm 7.2 mm	1000 μm 7.3 mm	1000 μm 7.3 mm

Table 14: Resolution (upper row) and cluster width (lower row) in $r\varphi$, $\theta = 6°$, $P_t = 200$ MeV/c, $R_{pad} = 240$ cm.

PRF width mm	Pad pitch mm			
	2.5	3.5	4.5	5.5
2.5	810 μm 5.4 mm	810 μm 5.5 mm	810 μm 5.6 mm	820 μm 5.6 mm
3.5	810 μm 5.9 mm	810 μm 6.0 mm	810 μm 6.0 mm	820 μm 6.1 mm
4.5	800 μm 6.5 mm	800 μm 6.6 mm	810 μm 6.6 mm	810 μm 6.6 mm
5.5	800 μm 7.1 mm	800 μm 7.2 mm	810 μm 7.3 mm	810 μm 7.3 mm

Table 15: Resolution (upper row) and cluster width (lower row) in $r\varphi$, $\theta = 6°$, $P_t = 100$ MeV/c, $R_{pad} = 110$ cm.

PRF width mm	Pad pitch mm			
	2.5	3.5	4.5	5.5
2.5	1880 μm 8.5 mm	1870 μm 8.6 mm	1870 μm 8.6 mm	1880 μm 8.6 mm
3.5	1860 μm 8.9 mm	1860 μm 8.9 mm	1860 μm 8.9 mm	1860 μm 9.0 mm
4.5	1850 μm 9.3 mm	1870 μm 9.3 mm	1850 μm 9.4 mm	1850 μm 9.4 mm
5.5	1850 μm 9.7 mm	1870 μm 9.8 mm	1850 μm 9.7 mm	1850 μm 9.9 mm

Table 16: Resolution (upper row) and cluster width (lower row) in $r\varphi$, $\theta = 6°$, $P_t = 100$ MeV/c, $R_{pad} = 240$ cm.